Surface warming and wetting due to methane's longwave radiative effects muted by shortwave absorption

Robert J. Allen[1], Xueying Zhao[1], Cynthia A. Randles[2,3], Ryan J. Kramer[4,5], Bjørn H. Samset[6] and Christopher J. Smith[7,8]

[1] *Department of Earth and Planetary Sciences, University of California Riverside, Riverside, CA, USA*

[2] *ExxonMobil Technology and Engineering Company, Annandale, NJ, USA*

[3] *now at UNEP International Methane Emission Observatory, Paris, France*

[4] *Climate and Radiation Laboratory, NASA Goddard Space Flight Center, Greenbelt, MD, USA*

[5] *Goddard Earth Science Technology and Research II, University of Maryland at Baltimore County, Baltimore MD, USA*

[6] *CICERO Center for International Climate and Environmental Research in Oslo, Oslo, Norway*

[7] *School of Earth and Environment, University of Leeds, Leeds, UK*

[8] *International Institute for Applied Systems Analysis (IIASA), Laxenburg, Austria*

Corresponding author email: rjallen@ucr.edu

Although greenhouse gases primarily absorb longwave radiation, they also absorb shortwave radiation. Recent studies have highlighted the importance of methane shortwave absorption, which enhances its stratospherically adjusted radiative forcing by up to ∼15%. The corresponding climate impacts, however, have only been indirectly evaluated and thus remain

largely unquantified. Here, we present a systematic, unambiguous analysis using one model and separate simulations with and without methane shortwave absorption. We find that methane shortwave absorption counteracts ∼30% of the surface warming associated with its longwave radiative effects. An even larger impact occurs for precipitation, as methane shortwave absorption offsets ∼60% of the precipitation increase relative to its longwave radiative effects. The methane shortwave-induced cooling is largely due to cloud rapid adjustments, including increased low-level clouds which enhance the reflection of incoming shortwave radiation, and decreased high-level clouds which enhance outgoing longwave radiation. The cloud responses, in turn, are related to the profile of atmospheric solar heating and corresponding changes in temperature and relative humidity. Despite our findings, methane remains a potent contributor to global warming and efforts to reduce methane emissions are vital for keeping global warming well below 2°C above preindustrial values.

The atmospheric concentration of methane (CH_4) has increased by about a factor of 2.4 since preindustrial times (from ∼0.75 to 1.8 parts per million by volume, ppm), resulting in an effective radiative forcing (ERF; Methods) of 0.496±0.099 W m^{-2} (from 1850 to 2019)[1], with similar estimates based on the stratospherically adjusted radiative forcing (SARF; Methods)[2–4]. Due to methane's potency as a greenhouse gas (i.e., its global warming potential, GWP, is 27.9 times stronger than CO_2 on a 100-year time horizon[5]), its relatively short lifetime (∼decade), and chemical reactions in the atmosphere (e.g., tropospheric ozone production), considerable interest exists in targeting CH_4 emissions to mitigate climate change and to improve air quality[4,6–13].

Recent studies[14–17] have highlighted the importance of CH_4 shortwave (SW) absorption at near-infrared wavelengths—which is lacking in many climate models[18]—resulting in up to a $\sim$15% increase in its SARF compared to the longwave (LW) SARF[19]. A more recent study[20] found a smaller increase in SARF at 7%, which was attributed, in part, to the inclusion of CH_4 absorption of solar mid-infrared radiation in the 7.6 μm band spectral region, which mainly impacts stratospheric absorption. The reduced forcing is because this spectral region mainly impacts stratospheric absorption. CH_4 SW absorption has regional "hot-spots", including near bright surfaces (e.g., deserts) and above clouds (e.g., oceanic stratus cloud decks)[21]. Such bright regions enhance the upward reflection of sunlight, which in turn enhances top-of-the-atmosphere (TOA) and tropopause CH_4 SW instantaneous radiative forcing (IRF). Considerable uncertainty exists, however, as this forcing is dependent on several quantities, including the cloud radiative effect, CH_4 vertical profile[20], and surface albedo specification[20]. In particular, large spatial gradients in the SW forcing are caused by near-infrared surface albedo[21].

These studies largely focus on how CH_4 SW absorption impacts its radiative forcing, with some also addressing the corresponding rapid adjustments (surface temperature-independent responses). For example, CO_2 and CH_4 (with SW absorption) fixed sea surface temperatures (SST) and slab ocean simulations were compared to show that rapid adjustments associated with CH_4 SW radiative effects act to mute precipitation increases[16], due to enhanced warming of the upper troposphere and lower stratosphere (UTLS). Methane SW rapid adjustments were also investigated in Precipitation Driver and Response Model Intercomparison Project (PDRMIP)[22] simulations. Models that lack CH_4 SW absorption yield a positive overall rapid adjustment (acting to increase net energy into the climate system), whereas models that include CH_4 SW absorption yield a negative overall rapid adjustment (acting to increase net energy out of the climate system)[18]. This difference is due to a more negative tropospheric temperature adjustment, and negative as opposed to positive stratospheric and cloud adjustments in models that include CH_4 SW absorption. These negative adjustments, in turn, are consistent with stronger UTLS warming, which promotes enhanced outgoing LW radiation (OLR) to space and high-level cloud reductions, which further promote enhanced OLR. Although other model differences (e.g., cloud parameterizations, CH_4 vertical profile, etc.) may impact this result, the implication is that CH_4 SW absorption may not lead to additional surface warming.

Although the importance of CH_4 SW absorption has been recognized, a comprehensive (and systematic) analysis of how it impacts the climate system remains to be conducted. Here, we perform experiments to rigorously assess CH_4 SW radiative impacts on the climate system, including rapid adjustments, surface temperature mediated feedbacks and the overall climate response.

Results

A suite of idealized methane-only time-slice perturbation simulations (Table 1; Methods) are conducted with the National Center for Atmospheric Research (NCAR) Community Earth System Model version 2.1.3 (CESM2)[23]. CESM2 includes the newest model components, including the Community Atmosphere Model version 6 (CAM6). Unlike many climate models[18], CAM6 includes CH_4 SW absorption in the near-infrared bands except the mid-infrared band in its radiative transfer parameterization. For each methane perturbation (2x, 5x and 10x preindustrial atmospheric CH_4 concentrations) considered and ocean boundary condition (fixed climatological sea surface temperatures, fSST, versus coupled ocean), we conduct pairs of identical experiments, one that includes CH_4 LW+SW radiative effects and one that lacks CH_4 SW radiative effects (Table 1). This allows quantification of the response signals (relative to preindustrial CH_4) to CH_4 LW+SW, LW and SW radiative effects, abbreviated as CH_{4LW+SW}, CH_{4LW} and CH_{4SW}, respectively. Under radiative transfer experiments (Methods), CH_4 radiative effects include the IRF only (i.e., the initial perturbation to the radiation balance). Under fSST experiments, CH_4 radiative effects can induce an ERF, which includes both the IRF and rapid adjustments (change in state in response to IRF, but excluding changes in sea-surface temperatures). Rapid adjustments can be LW adjustments (e.g., tropospheric and stratospheric temperatures), SW adjustments (surface albedo) or both SW and LW adjustments (clouds). The coupled ocean-atmosphere experiments quantify the total climate response, including the IRF, rapid adjustments, and the slow, surface temperature mediated effects.

Methane SW versus LW Total Climate Responses

Figure 1 shows the global mean change in near-surface air temperature and precipitation in coupled ocean-atmosphere CESM2 simulations which is the total response (including IRF, adjustments and surface temperature mediated feedbacks) to increases in atmospheric methane concentrations, including 2x, 5x and 10xCH_4 relative to preindustrial (see also Extended Data Figures 1-2). For all three perturbations, CH_{4LW}−which represents the total climate response to methane LW IRF, adjustments and feedbacks−yields an increase in near-surface air temperature and precipitation (i.e., warming and "wetting"). Significant global mean warming of 0.09, 0.68 and 1.24 K occurs for 2x, 5x and 10xCH_{4LW}; similarly, global wetting of 0.001 (not significant at the 90% confidence level), 0.035 and 0.063 mm day^{-1} occurs (corresponding precipitation percent changes are 0.04, 1.2 and 2.1%). Interestingly, CH_{4LW+SW}—which represents the total climate response to methane LW+SW IRF, adjustments and feedbacks—yields muted warming and wetting (except for 2xCH_{4LW+SW}). This is due to SW effects (including the IRF, adjustments and feedbacks), where significant global cooling occurs for 5x and 10xCH_{4SW} at -0.23 and -0.39 K. Similarly, a significant decrease in global mean precipitation occurs under these two methane perturbations at -0.021 and -0.039 mm day^{-1} (-0.7 and -1.3%). Most of the precipitation decrease occurs over tropical oceans (e.g., Extended Data Figure 2c).

The decrease in precipitation is consistent with atmospheric energetic constraints—in the global mean, the primary balance is between net atmospheric radiative cooling and condensational heating from precipitation[16,24–26]. As atmospheric shortwave absorption increases, net radiative cooling decreases, which is consistent with a decrease in precipitation. Except for the 2xCH_4 perturbation, CH_{4SW} offsets over $\sim$30% of the surface warming and $\sim$60% of the wetting associated with CH_{4LW}, i.e., SW absorption offsets twice as much of the precipitation increase, as compared to the surface warming.

We estimate the present-day CH_4 climate response (ΔCH_4 of 1.1 ppm) from least-squares regressions applied to our idealized 2x, 5x and 10xCH_4 simulations (i.e., Fig. 1a,b). Figure 1c shows the corresponding near-surface air temperature response, decomposed into CH_{4LW+SW}, CH_{4LW} and CH_{4SW}. We find global warming of 0.17 K in response to present-day CH_4 (relative to preindustrial); this is decomposed into warming of 0.20 K from CH_{4LW}, and cooling of -0.04 K from CH_{4SW}. Our estimate of 0.17 K for CH_{4LW+SW} is less than that given in the newest IPCC report (based on 2019 relative to 1750 and a two-layer emulator) at 0.28 K, with a 5-95% range of 0.19 to 0.39 K[1] (discussed in Supplementary Note 1). For global mean precipitation (Fig. 1d), precipitation increases of 0.16% and 0.31% occur for CH_{4LW+SW} and CH_{4LW}, respectively; drying of -0.15% occurs under CH_{4SW}. The apparent hydrological sensitivities (defined as the change in precipitation divided by the change in surface temperature)[27] are 0.97, 1.51 and 4.3% K^{-1} for CH_{4LW+SW}, CH_{4LW} and CH_{4SW}, respectively (Fig. 1e; discussed in Supplementary Note 2). Our decomposition helps to explain the larger apparent hydrological sensitivity to methane found in PDRMIP models (many of which lack CH_4 SW radiative effects; discussed in Supplementary Note 2).

Radiative Flux Components

To understand the cause of the CH_{4SW} surface cooling in coupled simulations, we evaluate the radiative flux components (Methods)−including ERF, IRF, and the rapid adjustments (ADJ)−in the fSST experiments. Figure 2a shows the TOA radiative flux components in response to $10xCH_{4LW+SW}$, $10xCH_{4LW}$ and $10xCH_{4SW}$. The IRF is 2.08 W m^{-2}, with $10xCH_{4LW}$ and $10xCH_{4SW}$ both contributing positive values at 1.81 and 0.27 W m^{-2}, respectively. Thus, the $10xCH_{4SW}$ IRF increases the $10xCH_{4LW}$ IRF by 15% (13% for 5x and $2xCH_4$). A prior study found a similar 15% increase under a 750 to 1800 ppb CH_4 perturbation[20]. A smaller increase of 6% was found at the tropopause[19], but the partitioning of SW IRF and LW IRF at the tropopause will differ from the TOA[17]. We also note that the presence of clouds increase the $10xCH_{4SW}$ IRF from 0.20 W m^{-2} under clear-sky conditions to 0.27 W m^{-2} under all-sky conditions (a 35% increase; $5xCH_{4SW}$ and $2xCH_{4SW}$ yield

27% and 33% increases, respectively). The increased forcing due to clouds is related to increased absorption path lengths in the CH_4 bands caused by multiple scattering[19,21].

The $10xCH_{4SW+LW}$ and $10xCH_{4LW}$ ERFs are also positive at 1.69 and 2.13 W m^{-2}, respectively, but negative under $10xCH_{4SW}$ at -0.44 W m^{-2}. Thus, $10xCH_{4SW}$ acts to reduce the $10xCH_{4LW}$ ERF by 21%. The difference between ERF and IRF is due to rapid adjustments (ADJ). $10xCH_{4SW+LW}$ yields a negative ADJ at -0.40 W m^{-2}, which is entirely due to $10xCH_{4SW}$ at -0.77 W m^{-2} (relative to the positive ADJ for $10xCH_{4LW}$ at 0.37 W m^{-2}). Thus, $10xCH_{4SW}$ drives a strong negative rapid adjustment, offsetting its smaller positive IRF (by about a factor of 3), leading to a negative ERF of -0.44 W m^{-2}. This $10xCH_{4SW}$ negative ERF is consistent with the corresponding decrease in near-surface air temperature previously discussed (Fig. 1). We note that some of the $10xCH_{4SW}$ adjustments are LW adjustments (discussed below).

Qualitatively similar results are obtained from $5xCH_4$ and $2xCH_4$ (Supplementary Note 3; Extended Data Figure 3). Atmospheric and surface radiation contributions to the TOA radiation (i.e., ERF) changes are discussed in Supplementary Note 4 (see also Supplementary Figure 1).

Rapid Adjustment Decomposition

To further understand the rapid adjustments and climate impacts of CH_4 SW absorption, Figure 2b shows the decomposition of TOA rapid adjustments (for $10xCH_4$) into the tropospheric temperature, stratospheric temperature, surface temperature, water vapor, albedo, and cloud adjustment (Methods). Clouds are the main driver of the relatively large negative $10xCH_{4SW}$ rapid adjustment. The corresponding cloud adjustment is -0.58 W m^{-2}, which is 75% of the total rapid adjustment. The stratospheric temperature adjustment also contributes at -0.15 W m^{-2}, as well as the tropospheric temperature adjustment at -0.11 W m^{-2}. The water vapor adjustment—at 0.10 W m^{-2}—acts to oppose these negative adjustments. The remaining rapid adjustments, including surface temperature and albedo, are relatively small. Similar results are obtained for 5x and 2xCH_4 (Extended Data Figure 4).

The 10xCH_{4SW} cloud adjustment (Fig. 2b) is due to both SW radiation at -0.42 W m^{-2} (Extended Data Figure 4c), as well as LW radiation at -0.16 W m^{-2} (Extended Data Figure 4b). The corresponding 10xCH_{4SW} temperature and water vapor adjustments are consistent with atmospheric warming (particularly in the UTLS; Figure 3b), which leads to enhanced outgoing LW radiation (a negative LW adjustment; Extended Data Figure 4b); the warming likewise increases water vapor (a greenhouse gas) which acts to decrease outgoing LW radiation (a positive LW adjustment; Extended Data Figure 4b). Supplementary Note 5 discusses the decomposition of surface (and atmospheric) rapid adjustments for 10xCH_4 (see also Supplementary Figure 2).

Recent analyses[3,18] have shown similar results across different kernels[28–30], including the GFDL kernel used here. Nonetheless, we repeat our rapid adjustment calculations with the CloudSat/CALIPSO[30] radiative kernel and find similar results (discussed in Supplementary Note 6; Extended Data Figure 5).

Understanding the Cloud Adjustment

The negative 10xCH_{4SW} cloud adjustment—including negative TOA SW and LW contributions—is consistent with the change in the global mean vertical profile of cloud cover (Figure 3d; dashed line). This includes increased low level cloud cover (peaking at 800 hPa) and enhanced reflection of SW radiation (a negative adjustment), but decreased high level cloud cover (peaking at 100 hPa) and enhanced outgoing LW radiation (a negative adjustment). The change in the vertical profile of cloud cover is related to the change in relative humidity (RH), which increases below $\sim$500 hPa, but decreases aloft (Fig. 3c; dashed line). The corresponding correlation, r, from the surface up to the lower stratosphere (up to $\sim$100 hPa) is 0.86, suggesting an increase (decrease) in RH is associated with more (less) clouds. The change in RH is consistent with the change in the vertical profile of temperature (r = -0.76; Fig. 3b; dashed line), which in turn is related to the atmospheric SW heating rate (r = 0.88; 3a; dashed line). Thus, we suggest the $10xCH_{4SW}$ cloud response is ultimately driven by the atmospheric SW heating rate profile, which decreases in the low/mid troposphere (below $\sim$700 hPa) but increases aloft, peaking in the UTLS at 100 hPa. This is consistent with the traditionally-defined aerosol-cloud semi-direct effect[31–34], whereby solar heating (e.g., from black carbon) increases atmospheric temperature and decreases RH, leading to cloud burn-off (with the opposite occurring in the lower troposphere). Atmospheric cooling below $\sim$800 hPa and warming aloft also imply an increase in stability, which is also likely associated with the increase in low cloud cover. Similar responses occur under $5xCH_4$ (Supplementary Figure 3) and (although weaker) $2xCH_4$ (Supplementary Figure 4).

Atmospheric Shortwave Heating Response Profile

The global annual mean CH_4 instantaneous SW heating rate response profile is not related to the vertical profile of the CH_4 concentration, which in CESM2/CAM6 has a uniform distribution in the troposphere (up to $\sim$200 hPa) and then exponentially decreases aloft (Extended Data Figure

6), consistent with chemical destruction of CH_4 above the tropopause. Instead, the instantaneous SW heating rate response profile is related to overlap of the three CH_4 SW absorption bands with water vapor. Under clear-sky conditions, with water vapor SW absorption in the three methane SW bands (Methods) turned off (using PORT), the vertical profile of CH_4 SW instantaneous absorption is relatively uniform in the troposphere, peaking in the UTLS (Figure 4a). Adding back the SW absorption by water vapor leads to the characteristic SW heating rate response profile (as in Fig.3a), with decreases in the lower troposphere and increases aloft, peaking in the UTLS. As expected, the 10xCH_{4SW} clear-sky IRF increases (from 0.20 to 0.40 W m^{-2}) when the overlapping SW absorption by water vapor is turned off.

Since water vapor is at its maximum in the lower troposphere, these SW absorption bands are already highly saturated in the lower atmosphere at preindustrial CH_4 concentrations, so perturbing methane does not lead to an increase in SW heating here. However, methane SW radiative effects enhance SW absorption aloft (increase in SW heating rate). This reduces the amount of solar radiation in these 3 bands that can be subsequently absorbed by water vapor in the lower troposphere, which results in the SW heating rate decrease below $\sim$700 hPa. Similar results are obtained under all-sky conditions (Fig. 4b). The 10xCH_{4SW} IRF increases (from 0.27 to 0.43 W m^{-2}) when the overlapping SW absorption by water vapor is turned off. Here, however, even with water vapor SW absorption (in the three methane bands) tuned off, there is still a decrease in the instantaneous SW heating rate near 800 hPa. This appears to be related to clouds, which peak at about the same level. Extended Data Figure 7 shows similar plots but based on three different latitude bands, including the low-latitudes (30°S-30°N); mid-latitudes (30°-60°N and 30°-60°S) and the high-latitudes (60°-90°N and 60°-90°S). There are some differences relative to the global mean (Fig. 4), but the results are generally similar. For example, absorption by water vapor (in the three methane bands) is more important in the low-latitudes (Extended Data Figure 7e), consistent with the larger amount of water vapor (specific humidity) in the tropics. To summarize, methane SW instantaneous radiative effects result in a vertical redistribution of atmospheric SW heating, with enhanced SW heating aloft (maximizing in the UTLS), but decreased SW heating in the lower troposphere. This, in turn, leads to the corresponding cloud cover changes (increased low-level but decreased high-level cloud cover) and negative cloud adjustment, through modification of atmospheric temperature and relative humidity.

Climate Feedbacks under Methane SW Radiative Effects

Figure 5 shows the radiative kernel decomposition applied to the coupled ocean-atmosphere simulations for 10xCH_{4SW} (5x and 2xCH_{4SW} are included in Supplementary Figure 5). We also include the previously discussed rapid adjustments (i.e., “fast” responses from the fSST runs), and the difference between the coupled and fSST decompositions (i.e., the surface temperature-induced “slow” feedbacks). Note that we do not normalize our feedbacks by the change in global mean surface temperature; unnormalized feedbacks facilitate comparison to the rapid adjustments. Thus, positive/negative feedbacks have the same meaning as positive/negative rapid adjustments (i.e., positive is an increase in net energy; negative is a decrease in net energy).

In most cases, the slow feedback dominates the sign of the overall response, consistent with the climate system acting to restore TOA radiative equilibrium. For example, the slow tropospheric temperature feedback is positive at 1.14 W m^{-2} (which is offset to some extent by the water vapor feedback at -0.62 W m^{-2}). Both of these feedbacks are consistent with tropospheric cooling (Supplementary Figure 6b). For clouds, however, the rapid adjustment and the slow feedback are both negative, with a larger value for the rapid adjustment at -0.58 vs. -0.37 W m^{-2}. Thus, the surface cooling in response to CH_4 SW radiative effects is largely due to cloud rapid adjustments, but surface-temperature induced cloud feedbacks also act to cool the planet.

The 10xCH_{4SW} cloud feedback is dominated by increases in low-level (and mid-level clouds), with weaker decreases in high-level clouds (Supplementary Figure 6d; discussed in Supplementary Note 7). Similar results exist for 5xCH_{4SW} (Supplementary Figure 7), but weaker results exist for 2xCH_{4SW} (Supplementary Figure 8; Supplementary Note 7).

Conclusions

Using targeted climate model simulations, we have shown that methane SW absorption and the associated rapid adjustments act to reduce its ERF by $\sim$20%, and mute its warming and wetting effects in coupled simulations by up to 30% and 60%, respectively. Similar simulations with additional climate models are needed to understand the robustness of the results presented here−particularly since the CH_4 SW IRF is dependent on uncertain quantities, like the cloud radiative effect[21], surface albedo[20,21] and the CH_4 vertical profile[20]. However, the indirect assessment of multiple models from PDRMIP CH_4 simulations supports our findings[18]. In fact, expanding upon the results of ref.[18], we find a 20% decrease in ERF, 45% less warming and 65% less wetting in models that include CH_4 SW absorption versus those that do not (discussed in Supplementary

Note 8; Extended Data Figure 8).

Although the SW radiative effects to the present-day methane perturbation remain relatively small, they could be quite large by the end of the century−Shared Socio-economic Pathway (SSP) 3-7.0, which lacks climate policy and has “weak” levels of air quality control measures[7,35,36], features end-of-century increases of CH_4 concentrations approaching 5x preindustrial (i.e., 3.4 ppm). Overall, methane remains a potent contributor to global warming and emission reductions are a vital component of climate change mitigation policies, and for continued pursuit of the climate goals laid out under the Paris Agreement.

Acknowledgements: R. J. Allen is supported by NSF grant AGS-2153486 and the Research Council of Norway Project No. 324182. R. Kramer is supported by NASA Science of Terra, Aqua and Suomi-NPP grant no. 80NSSC21K1968 and NOAA grant no. NA18OAR4310269. We would like to acknowledge high-performance computing support from Cheyenne (doi:10.5065/D6RX99HX) provided by NCAR’s Computational and Information Systems Laboratory, sponsored by the National Science Foundation.

Author Contributions: R. J. Allen conceived the project, designed the study, performed simulations and analyses and wrote the paper. X. Zhao performed preliminary simulations. C. A. Randles, R. J. Kramer, C. J. Smith and B. H. Samset advised on methods and data interpretation. All authors discussed results and contributed to the writing of the manuscript.

Competing Interests: The authors declare no competing interests.

Table 1: **Description of CESM2/CAM6 methane experiments.** Top half of table shows model experiments; bottom half shows response signals (i.e., difference of experiments). Atmospheric methane concentrations are perturbed relative to the preindustrial (PI = year 1850) concentration. 10xCH_4 (preindustrial) represents 7.9 (0.79) parts per million by volume (ppm). Experiments are performed with both fixed climatological sea surface temperatures and a coupled ocean. The former allows quantification of the rapid adjustments/fast responses; the latter allows quantification of the total climate response. The difference (total climate response minus fast response) quantifies the slow, surface temperature mediated feedback response.

Experiments	Description
^{a}10xCH_4^{EXP}	10xCH_4 with CH_4 LW+SW radiative effects
^{a}10xCH_{4NOSW}^{EXP}	10xCH_4 with CH_4 SW radiative effects turned off (i.e., LW effects)
PI^{EXP}	Preindustrial CH_4 with CH_4 LW+SW radiative effects
PI_{NOSW}^{EXP}	Preindustrial CH_4 with SW radiative effects turned off (i.e., LW effects)
Signal	**Description**
10xCH_{4LW+SW} = 10xCH_4^{EXP} $-$ PI^{EXP}	Response to CH_4 LW+SW radiative effects^{b}
10xCH_{4LW} = 10xCH_{4NOSW}^{EXP} $-$ PI_{NOSW}^{EXP}	Response to CH_4 LW radiative effects^{b}
10xCH_{4SW} = (10x$CH_4^{EXP}$$-$$PI^{EXP}$) $-$ (10x$CH_{4NOSW}^{EXP}$$-$$PI_{NOSW}^{EXP}$)	Response to CH_4 SW radiative effects^{b}

^{a}Analogous sets simulations are also conducted for both 5x (3.95 ppm) and 2x (1.58 ppm) CH_4.

^{b}Radiative effects include IRF for radiative transfer simulations; IRF and rapid adjustments$-$which can be LW and SW adjustments$-$for fSST simulations; and IRF, rapid adjustments and feedbacks for coupled simulations.

1. Forster, P. *et al.* The Earth's Energy Budget, Climate Feedbacks, and Climate Sensitivity. In Climate Change 2021: The Physical Science Basis. Contribution of Working Group I to the Sixth Assessment Report of the Intergovernmental Panel on Climate Change [Masson-Delmotte, V., P. Zhai, A. Pirani, S.L. Connors, C. Péan, S. Berger, N. Caud, Y. Chen, L. Goldfarb, M.I. Gomis, M. Huang, K. Leitzell, E. Lonnoy, J.B.R. Matthews, T.K. Maycock, T. Waterfield, O. Yelekçi, R. Yu, and B. Zhou (eds.)]. Tech. Rep., Cambridge University Press, Cambridge, United Kingdom and New York, NY, USA, pp. 923-1054, doi: :10.1017/9781009157896.009 (2021).

2. Myhre, G. *et al.* Anthropogenic and Natural Radiative Forcing. In: Climate Change 2013: The Physical Science Basis. Contribution of Working Group I to the Fifth Assessment Report of the Intergovernmental Panel on Climate Change [Stocker, T.F., D. Qin, G.-K. Plattner, M. Tignor, S.K. Allen, J. Boschung, A. Nauels, Y. Xia, V. Bex and P.M. Midgley (eds.)]. Tech. Rep., Cambridge University Press, Cambridge, United Kingdom and New York, NY, USA (2013).

3. Thornhill, G. D. *et al.* Effective radiative forcing from emissions of reactive gases and aerosols – a multi-model comparison. *Atmospheric Chemistry and Physics* **21**, 853–874, doi: 10.5194/acp–21–853–2021 (2021).

4. Szopa, S. *et al.* Short-Lived Climate Forcers. In Climate Change 2021: The Physical Science Basis. Contribution of Working Group I to the Sixth Assessment Report of the Intergovernmental Panel on Climate Change [Masson-Delmotte, V., P. Zhai, A. Pirani, S.L. Connors, C. Péan, S. Berger, N. Caud, Y. Chen, L. Goldfarb, M.I. Gomis, M. Huang, K. Leitzell, E. Lon-

noy, J.B.R. Matthews, T.K. Maycock, T. Waterfield, O. Yelekçi, R. Yu, and B. Zhou (eds.)]. Tech. Rep., Cambridge University Press, Cambridge, United Kingdom and New York, NY, USA, pp. 817–922, doi:10.1017/9781009157896.008 (2021).

5. Smith, C. *et al.* The Earth's Energy Budget, Climate Feedbacks, and Climate Sensitivity Supplementary Material. In: Climate Change 2021: The Physical Science Basis. Contribution of Working Group I to the Sixth Assessment Report of the Intergovernmental Panel on Climate Change [Masson-Delmotte, V., P. Zhai, A. Pirani, S. L. Connors, C. Péan, S. Berger, N. Caud, Y. Chen, L. Goldfarb, M. I. Gomis, M. Huang, K. Leitzell, E. Lonnoy, J.B.R. Matthews, T. K. Maycock, T. Waterfield, O. Yelekçi, R. Yu and B. Zhou (eds.)]. Tech. Rep., Cambridge University Press, Cambridge, United Kingdom and New York, NY, USA (2021).

6. Collins, W. J. *et al.* AerChemMIP: quantifying the effects of chemistry and aerosols in CMIP6. *Geoscientific Model Development* **10**, 585–607, doi: 10.5194/gmd–10–585–2017 (2017).

7. Allen, R. J. *et al.* Significant climate benefits from near-term climate forcer mitigation in spite of aerosol reductions. *Environmental Research Letters* **16**, 034010, doi: 10.1088/1748–9326/abe06b (2021).

8. Hayman, G. D. *et al.* Regional variation in the effectiveness of methane-based and land-based climate mitigation options. *Earth System Dynamics* **12**, 513–544, doi: 10.5194/esd–12–513–2021 (2021).

9. United Nations Environment Programme and Climate and Clean Air Coalition. Global Methane Assessment: Benefits and Costs of Mitigating Methane Emissions. Tech. Rep.,

Nairobi: United Nations Environment Programme (2021).

10. Cain, M. *et al.* Methane and the Paris Agreement temperature goals. *Philos Trans A Math Phys Eng Sci.* **380(2215): 20200456**, doi: 10.1098/rsta.2020.0456 (2022).

11. Mar, K. A., Unger, C., Walderdorff, L. & Butler, T. Beyond CO2 equivalence: The impacts of methane on climate, ecosystems, and health. *Environmental Science & Policy* **134**, 127–136, doi: 10.1016/j.envsci.2022.03.027 (2022).

12. Turnock, S. T. *et al.* The future climate and air quality response from different near-term climate forcer, climate, and land-use scenarios using UKESM1. *Earth's Future* **10**, e2022EF002687, doi: 10.1029/2022EF002687 (2022).

13. Hassan, T. *et al.* Air quality improvements are projected to weaken the Atlantic meridional overturning circulation through radiative forcing effects. *Communications Earth & Environment* **3**, 149, doi: 10.1038/s43247–022–00476–9 (2022).

14. Collins, W. D. *et al.* Radiative forcing by well-mixed greenhouse gases: Estimates from climate models in the Intergovernmental Panel on Climate Change (IPCC) Fourth Assessment Report (AR4). *Journal of Geophysical Research: Atmospheres* **111**, doi: 10.1029/2005JD006713 (2006).

15. Li, J., Curry, C. L., Sun, Z. & Zhang, F. Overlap of solar and infrared spectra and the short-wave radiative effect of methane. *Journal of the Atmospheric Sciences* **67**, 2372–2389, doi: 10.1175/2010JAS3282.1 (2010).

16. Modak, A., Bala, G., Caldeira, K. & Cao, L. Does shortwave absorption by methane influence its effectiveness? *Climate Dynamics* **51**, 3653–3672, doi: 10.1007/s00382–018–4102–x (2018).

17. Shine, K. P., Byrom, R. E. & Checa-Garcia, R. Separating the shortwave and longwave components of greenhouse gas radiative forcing. *Atmospheric Science Letters* **23**, e1116, doi: 10.1002/asl.1116 (2022).

18. Smith, C. J. *et al.* Understanding rapid adjustments to diverse forcing agents. *Geophysical Research Letters* **45**, 12023–12031, doi: 10.1029/2018GL079826 (2018).

19. Etminan, M., Myhre, G., Highwood, E. J. & Shine, K. P. Radiative forcing of carbon dioxide, methane, and nitrous oxide: A significant revision of the methane radiative forcing. *Geophysical Research Letters* **43**, 12,614–12,623, doi: 10.1002/2016GL071930 (2016).

20. Byrom, R. E. & Shine, K. P. Methane's solar radiative forcing. *Geophysical Research Letters* e2022GL098270, doi: 10.1029/2022GL098270 (2022).

21. Collins, W. D., Feldman, D. R., Kuo, C. & Nguyen, N. H. Large regional shortwave forcing by anthropogenic methane informed by Jovian observations. *Science Advances* **4**, eaas9593, doi: 10.1126/sciadv.aas9593 (2018).

22. Myhre, G. *et al.* PDRMIP: A Precipitation Driver and Response Model Intercomparison Project—Protocol and Preliminary Results. *Bulletin of the American Meteorological Society* **98**, 1185–1198, 10.1175/BAMS–D–16–0019.1 (2017).

23. Danabasoglu, G. *et al.* The Community Earth System Model version 2 (CESM2). *Journal of Advances in Modeling Earth Systems* **12**, e2019MS001916, doi: 10.1029/2019MS001916 (2020).

24. Muller, C. J. & O'Gorman, P. A. An energetic perspective on the regional response of precipitation to climate change. *Nature Climate Change* **1**, 266–271, doi: 10.1038/nclimate1169 (2011).

25. Richardson, T. B. *et al.* Drivers of precipitation change: An energetic understanding. *Journal of Climate* **31**, 9641–9657, doi: 10.1175/JCLI–D–17–0240.1 (2018).

26. Liu, L. *et al.* A PDRMIP multimodel study on the impacts of regional aerosol forcings on global and regional precipitation. *Journal of Climate* **31**, 4429–4447, doi: 10.1175/JCLI–D–17–0439.1 (2018).

27. Fläschner, D., Mauritsen, T. & Stevens, B. Understanding the intermodel spread in global-mean hydrological sensitivity. *Journal of Climate* **29**, 801–817, doi: 0.1175/JCLI–D–15–0351.1 (2016).

28. Pendergrass, A. G., Conley, A. & Vitt, F. M. Surface and top-of-atmosphere radiative feedback kernels for CESM-CAM5. *Earth System Science Data* **10**, 317–324, doi: 10.5194/essd–10–317–2018 (2018).

29. Smith, C. J., Kramer, R. J. & Sima, A. The HadGEM3-GA7.1 radiative kernel: the importance of a well-resolved stratosphere. *Earth System Science Data* **12**, 2157–2168, doi: 10.5194/essd–12–2157–2020 (2020).

30. Kramer, R. J., Matus, A. V., Soden, B. J. & L'Ecuyer, T. S. Observation-based radiative kernels from CloudSat/CALIPSO. *Journal of Geophysical Research: Atmospheres* **124**, 5431–5444, doi: 10.1029/2018JD029021 (2019).

31. Allen, R. J. & Sherwood, S. C. The aerosol-cloud semi-direct effect and land-sea temperature contrast in a GCM. *Geophys. Res. Lett.* **37**, L07702, doi:10.1029/2010GL042759 (2010).

32. Koch, D. & Del Genio, A. D. Black carbon semi-direct effects on cloud cover: review and synthesis. *Atmos. Chem. Phys.* **10**, 7685–7696 (2010).

33. Amiri-Farahani, A., Allen, R. J., Li, K.-F. & Chu, J.-E. The semidirect effect of combined dust and sea salt aerosols in a multimodel analysis. *Geophysical Research Letters* **46**, 10512–10521, doi: 10.1029/2019GL084590 (2019).

34. Allen, R. J. *et al.* Observationally-constrained aerosol-cloud semi-direct effects. *npj Climate and Atmospheric Science* **2**, doi: 10.1038/s41612–019–0073–9 (2019).

35. Fujimori, S. *et al.* SSP3: AIM implementation of Shared Socioeconomic Pathways. *Global Environmental Change* **42**, 268–283, doi: 10.1016/j.gloenvcha.2016.06.009 (2017).

36. Gidden, M. J. *et al.* Global emissions pathways under different socioeconomic scenarios for use in CMIP6: a dataset of harmonized emissions trajectories through the end of the century. *Geoscientific Model Development* **12**, 1443–1475, doi: 10.5194/gmd–12–1443–2019 (2019).

Methods

a. Radiative Forcing Definitions

The Instantaneous Radiative Forcing (IRF) is the initial perturbation to Earth's radiation budget and does not account for rapid adjustments. We diagnose IRF using the Parallel Offline Radiative Transfer (PORT) model[37], which isolates the the Rapid Radiative Transfer Model for General circulation models (RRTMG)[38–40] radiative transfer computation from the CESM2-CAM6 model configuration (more details on RRTMG are presented below). PORT simulations are run for 16 months; the last 12 months are used to diagnose annual mean IRF. PORT is also used to verify our methodology to remove RRTMG CH_4 SW absorption (i.e., the SW IRF is zero in the CH_{4NOSW}^{EXP} and PI_{NOSW}^{EXP} experiments, and the LW IRF is unchanged).

The Effective Radiative Forcing (ERF) is defined as the net TOA radiative flux difference between the perturbed and base simulation, with climatological fixed SSTs and sea ice distributions and no correction for land surface temperature change[41]. We note that the contribution of land surface warming/cooling to the ERF in our simulations is relatively small ($<$5% of the ERF; see Supplementary Note 9). ERF can be decomposed into the sum of IRF and the rapid adjustments.

The stratospherically adjusted radiative forcing (SARF) is equal to the sum of the IRF and the stratospheric temperature adjustment. Thus, the difference between ERF and SARF is that ERF includes all adjustments, whereas SARF only includes the adjustment due to stratospheric temperature change[2,42,43].

b. CESM2/CAM6 Simulations

We conduct pairs of identical simulations, one that includes CH_4 LW+SW radiative effects (CH_4^{EXP}) and one that lacks CH_4 SW radiative effects (CH^{EXP}_{4NOSW}); Table 1). The latter simulations are conducted by turning off CH_4 SW absorption in the three near-infrared bands, including 1.6-1.9 μm, 2.15-2.5 μm and 3.1-3.85 μm in CAM6's radiative transfer parameterization (RRTMG). RRTMG does not include methane SW absorption in the mid-infrared band at 7.6 μm. The sign of the CH_4 SW IRF (at the tropopause) depends on the increased absorption in the troposphere, since the downward SW flux at the tropopause is always decreased due to absorption in the stratosphere[19]. Including the 7.6 μm band primarily increases CH_4 SW absorption in the stratosphere[20]. This reduces the forcing from the downward irradiance, with negligible change to the forcing from the upward irradiance, i.e., the tropopause SW IRF is reduced. Thus, if RRTMG included the 7.6 μm methane band, we would expect the CH_4 SW IRF at the TOA to increase due to the increase in stratospheric absorption. This, however, will result in a larger (negative) stratospheric temperature adjustment.

RRTMG is an accelerated and modified version of RRTM and uses the correlated k-distribution (CKD) method to treat gas absorption[40]. RRTMG calculates irradiance and heating rate in broad spectral intervals, while retaining a high level of accuracy relative to measurements and high-resolution line-by-line models. Sub-grid cloud characterization is treated in both the longwave and shortwave spectral regions with McICA, the Monte-Carlo Independent Column Approximation[44], using the maximum-random cloud overlap assumption. RRTMG divides the solar spectrum into 14 shortwave bands that extend over the spectral range from 0.2 μm to 12.2 μm. The infrared spectrum in RRTMG is divided into 16 longwave bands that extend over the spectral range from

3.1 μm to 1000.0 μm.

Few studies have evaluated broad-band radiative transfer codes against benchmark calculations, particularly for CH_4 SW IRF. This is in part because the radiation parameterization in many climate models lacks an explicit treatment of CH_4 SW absorption[14,18]. The 6-band SOCRATES SW spectral file configuration used in the Met Office Unified Model significantly underestimates CH_4 SW tropopause and surface IRF by around 45% compared to the 260-band configuration[20]. Similarly, RRTMG−the radiative transfer model used here−was recently found to underestimate CH_4 (and CO_2) SW IRF by 25-45%[45]. This implies that there are opportunities for improvement in the parts of the spectrum where the absorption by these gases is weak but not zero. Thus, incorporating CH_4 SW absorption in more models' radiative transfer codes is only part of the solution−making sure their radiative transfer codes have a validated treatment of SW absorption by CH_4 (and other greenhouse gases) is also vital. We also note that N_2O is not represented in the shortwave part of RRTMG.

The Community Land Model version 5 (CLM5)[46] provides both the surface albedo, area-averaged for each atmospheric column, and the upward longwave surface flux, which incorporates the surface emissivity, for input to the radiation. For the shortwave, the surface albedos are specified at every grid point at every time step. The albedos are partitioned into two wavebands (0.2-0.7 μm and 0.7-12.0 μm) for both direct and diffuse incident radiation[47]. Surface albedos for ocean surfaces, geographically varying land surfaces, and sea ice surfaces are distinguished. They depend on the solar zenith angle, the amount and optical properties of vegetation, and the optical properties of snow and soil [46].

Rapid adjustments−which can be SW or LW adjustments−are estimated by subtracting the preindustrial control (PI^{EXP}) fSST experiment from each perturbation fSST experiment. For example, to quantify the rapid adjustments in response to a ten fold increase in preindustrial atmospheric methane concentration, we take the 10xCH_4 fSST simulation minus the preindsustrial fSST simulation ($10xCH_4^{EXP}-PI^{EXP}$). This signal ($10xCH_{4LW+SW}$) includes the methane LW+SW IRF and its impact on LW and SW adjustments under the fSST boundary condition (i.e., ERF = IRF + adjustments). Rapid adjustments due to CH_4 LW IRF and its impact on LW and SW adjustments ($10xCH_{4LW}$) are estimated from $10xCH_{4NOSW}^{EXP} - PI_{NOSW}^{EXP}$. Similarly, rapid adjustments due to CH_4 SW IRF and the impact of CH_4 SW absorption on LW and SW adjustments (i.e., $10xCH_{4SW}$) are estimated from $(10xCH_4^{EXP}-PI^{EXP}) - (10xCH_{4NOSW}^{EXP}-PI_{NOSW}^{EXP})$. Specific details on how the rapid adjustments are estimated (i.e., via radiative kernels) are discussed below. A similar procedure is used to quantify the total climate impacts from the coupled ocean simulations, which include the IRF, adjustments and surface-temperature mediated feedbacks.

We note that an alternative experimental design where methane LW radiative effects are removed could be implemented. As our goal is to understand the impacts of adding CH_4 SW absorption (which many models lack) to the LW forcing (which model already have), our experimental design is based on the all-but-one type of experimental design. Our simulations therefore target the inclusion of CH_4 SW absorption, allowing quantification of its associated rapid adjustments and climate impacts. This is in contrast to the studies discussed above, which either evaluate CH_4 SW radiative effects by contrasting CH_4 versus CO_2 (which lacks strong SW absorption) simulations[16], or by comparing models that include CH_4 SW absorption versus models that do not[18]. In the latter, other model differences (e.g., cloud parameterizations, CH_4 vertical profile, etc.) may be important.

All CESM2/CAM6 simulations are conducted with a 1.9°x2.5° horizontal resolution and 32 vertical levels in the atmosphere. Fixed sea-surface temperature experiments are run for 32 years each, the last 30 of which are used to quantify ERF and the rapid adjustments/fast responses. Coupled ocean simulations are run for 90 years each, starting from a pre-spun up preindustrial control simulation in year 321. The last 40 years of the coupled experiments−when the net top-of-the-atmosphere radiative flux stabilizes−are used to quantify climate impacts. The surface temperature mediated slow response is calculated as the difference between coupled ocean and fSST experiments[48]. A 90-year coupled ocean simulation has not yet reached equilibrium, so we refer to these simulations as being in near-equilibrium (computational cost restrictions prohibited longer integrations), similar to prior projects including PDRMIP[22,49]. Our CESM2/CAM6 simulations do not include interactive chemistry; we therefore do not address possible atmospheric chemistry implications (e.g., changes in ozone and stratospheric water vapor) nor changes in methane lifetime.

c. Calculation of Rapid Adjustments

Rapid adjustments (e.g., clouds, water vapor, temperature) in the climatological fixed SST experiments are estimated using the radiative kernel method[3,18,28,30,43]. Radiative kernels represent the radiative impacts from small perturbations in a state variable (e.g., temperature, water vapor, and surface albedo). Subsequently, rapid adjustments can be computed by multiplication of the kernel with the response of the state variable. We use the Python-based radiative kernel toolkit (downloaded from `https://climate.rsmas.miami.edu/data/radiative-kernels/`) and the

Geophysical Fluid Dynamics Laboratory (GFDL) radiative kernel[50].

We use the same radiative kernel procedure to calculate the unnormalized (i.e., we do not divide by the change in global mean surface temperature) feedbacks. Specifically, surface temperature induced feedbacks are estimated by subtracting the rapid adjustments (from fixed SST experiments) from the corresponding radiative kernel decomposition applied to the coupled experiments. Unnormalized feedbacks facilitate comparison to the rapid adjustments.

ERF can be decomposed as: $ERF = IRF + ADJ_{TT} + ADJ_{ST} + ADJ_{TS} + ADJ_{WV} + ADJ_{\alpha} + ADJ_C + \epsilon$, where IRF is the instantaneous radiative forcing, ADJ_{TT} is the tropospheric temperature adjustment, ADJ_{ST} is the stratospheric temperature adjustment, ADJ_{TS} is the surface temperature adjustment, ADJ_{WV} is the water vapor adjustment, ADJ_{α} is the albedo adjustment, ADJ_C is the cloud adjustment and ϵ is the radiative kernel error. Individual rapid adjustments are estimated as $ADJ_x = \frac{\delta R}{\delta x} dx$, where $\frac{\delta R}{\delta x}$ is the radiative kernel and dx is the response of state variable x as simulated by CESM2/CAM6. Kernels are four-dimensional (latitude, longitude, pressure, month) fields for atmospheric temperature and specific humidity, and three-dimensional (latitude, longitude, month) for surface temperature and surface albedo. Two sets of kernels are used: clear-sky kernels, where the fluxes are calculated without clouds, and all-sky kernels.

As the radiative effect of clouds depends on several variables (fraction, ice and liquid water content, droplet effective radius, etc.), several approaches have been used to estimate cloud adjustments[18,51]. Here, we estimate cloud adjustments using the kernel difference method[18], which involves a cloud-masking correction of cloud radiative forcing diagnostics using the kernel-derived non-cloud adjustments and IRF according to: $ADJ_C = (ERF - ERF_{cs}) - (IRF - IRF_{cs}) - \sum_{x=[T,TS,WV,\alpha]} (ADJ_x - ADJ_{x,cs})$, where subscript "$cs$" refers to clear-sky quantities. Thus, the kernel difference method relies on the difference of all-sky and clear-sky kernel decompositions. See ref.[18] for additional details.

The total rapid adjustment is estimated as the sum of individual rapid adjustments from the radiative kernel decomposition. Since we estimate IRF using PORT for all of our methane simulations, this can be used to estimate the radiative kernel error (ϵ) as: $\epsilon = ERF - IRF - \sum_{x=[T,TS,WV,\alpha,C]}(ADJ_x)$. For example, the 10x$CH_{4LW+SW}$ ERF and IRF are 1.69 and 2.08 W m^{-2}, yielding an ERF$-$IRF difference of -0.39 W m^{-2}. The sum of the individual rapid adjustments from the kernel decomposition is -0.40 W m^{-2}. Thus, the radiative kernel error for 10xCH_{4LW+SW} is 0.01 W m^{-2}. Similar results hold for 5x and 2xCH_{4LW+SW}, where ϵ is 0.03 W m^{-2} and -0.02 W m^{-2}, respectively. Relative to the corresponding ERFs, these errors are $<$1%; 3.1%; and 5.7%, respectively. As ref.[18] lacked an estimate of the IRF (which we estimate using PORT), they estimated ϵ under select situations (i.e., where the SW or LW IRF is known to be zero). In these situations, they find that the residual term is small, being "6%, 12%, and 2% of the ERF for 10xBC LW, 3xCH_4 SW, and 2%Solar LW in magnitude, respectively. The larger multimodel residual in the 3xCH_4 SW case is biased by a large relative residual in the HadGEM2 model, whereas residuals in the other four models analyzed are close to 0." Thus, our radiative kernel errors are relatively small, and comparable to those estimated from select PDRMIP simulations[18].

We note that methane IRF has an approximate square root dependency on concentration[5,52]. PDRMIP 3xCH_4 simulations yield a 3xCH_4 IRF of 1.1$\pm$0.24 W m^{-2}, but nearly all of the PDRMIP models used year 2000 as the base year. This perturbation is thus similar to 5-6x preindustrial CH_4 (our 5xCH_4 IRF is 1.18 W m^{-2}, with 0.14 W m^{-2} due to SW radiative effects).

d. Statistical Significance

Statistical significance of a climate response is calculated using a two-tailed pooled t-test. An annual mean time series is calculated for both the perturbation experiment and the preindustrial base experiment (e.g., at individual grid boxes or averaged globally), and their difference is taken. The null hypothesis of a zero difference is evaluated, with $n_1 + n_2 - 2$ degrees of freedom, where n_1 and n_2 are the number of years in the perturbation experiment and base (i.e., 30 years for fSST experiments; 40 years for coupled ocean experiments). Here, the pooled variance, $\frac{(n_1-1)S_1^2+(n_2-1)S_2^2}{n_1+n_2-2}$, is used, where S_1 and S_2 are the sample variances.

A similar procedure is used to quantify statistical significance of the radiative flux perturbations and rapid adjustments (e.g., Fig.2). These uncertainties are therefore relative to interannual variability, and do not account for possible intermodel or kernel uncertainties (as in ref.[18], using 10+ PDRMIP models). As we only have 1 year of data for the IRF, we evaluate its uncertainty relative to the preindustrial base experiment with fixed SSTs. Nearly all of our rapid adjustments under 10xCH_4 are significant at the 90% confidence level (the lone exception is the surface temperature adjustment under 10xCH_{4SW}). Similar conclusions also hold for 5xCH_4 (Extended Data Figure 4d). Under 2xCH_4, however, most of the rapid adjustments under 2xCH_{4SW} are not significant (Extended Data Figure 4g), including the total rapid adjustment. This is consistent with the relatively small 2xCH_4 SW IRF at 0.04 W m^{-2}.

We also find similar results using an alternative kernel (CloudSat/CALIPSO; Extended Data Figure 5), so our rapid adjustment conclusions are robust across these two kernels. Finally, we note that the rapid adjustments in PDRMIP models that include CH_4 SW absorption (under 3xCH_4, which is a perturbation similar to our 5x preindustrial CH_4) are all significant at the 95% confidence level[18], and this includes the intermodel and kernel uncertainty.

Data Availability: PDRMIP simulations can be accessed at `https://cicero.oslo.no/en/PDRMIP/PDRMIP-data-access`. A core set of model data from our idealized methane CESM2 simulations can be downloaded from Zenodo at `https://doi.org/10.5281/zenodo.7596623`.

Code Availability: The Python-based radiative kernel toolkit and the GFDL radiative kernel can be downloaded from `https://climate.rsmas.miami.edu/data/radiative-kernels/`

Methods-only References

37. Conley, A. J., Lamarque, J.-F., Vitt, F., Collins, W. D. & Kiehl, J. PORT, a CESM tool for the diagnosis of radiative forcing. *Geoscientific Model Development* **6**, 469–476, doi: 10.5194/gmd–6–469–2013 (2013).

38. Mlawer, E. J. & Clough, S. A. Shortwave and longwave enhancements in the rapid radiative transfer model. In *Proceedings of the 7th Atmospheric Radiation Measurement (ARM) Science*

Team Meeting, US Department of energy, CONF-970365 (1998).

39. Clough, S. A. *et al.* Atmospheric radiative transfer modeling: A summary of the AER codes. *Journal of Quantitative Spectroscopy and Radiative Transfer* **91**, 233–244, doi:10.1016/j.jqsrt.2004.05.058 (2005).

40. Iacono, M. J. *et al.* Radiative forcing by long-lived greenhouse gases: Calculations with the AER radiative transfer models. *J. Geophys. Res.-Atmos.* **113**, D13103, doi: 10.1029/2008JD009944 (2008).

41. Forster, P. M. *et al.* Recommendations for diagnosing effective radiative forcing from climate models for CMIP6. *Journal of Geophysical Research: Atmospheres* **121**, 12,460–12,475, doi: 10.1002/2016JD025320 (2016).

42. Sherwood, S. C. *et al.* Adjustments in the forcing-feedback framework for understanding climate change. *Bulletin of the American Meteorological Society* **96**, 217–228, doi: 10.1175/BAMS–D–13–00167.1 (2015).

43. Smith, C. J. *et al.* Effective radiative forcing and adjustments in CMIP6 models. *Atmospheric Chemistry and Physics* **20**, 9591–9618, doi: 10.5194/acp–20–9591–2020 (2020).

44. Pincus, R., Barker, H. W. & Morcrette, J.-J. A fast, flexible, approximate technique for computing radiative transfer in inhomogeneous cloud fields. *Journal of Geophysical Research: Atmospheres* **108**, doi: 10.1029/2002JD003322 (2003).

45. Hogan, R. J. & Matricardi, M. Evaluating and improving the treatment of gases in radiation schemes: the Correlated K-Distribution Model Intercomparison Project (CKDMIP). *Geoscientific Model Development* **13**, 6501–6521, doi: 10.5194/gmd–13–6501–2020 (2020).

46. Lawrence, D. M. *et al.* The Community Land Model Version 5: Description of new features, benchmarking, and impact of forcing uncertainty. *Journal of Advances in Modeling Earth Systems* **11**, 4245–4287, doi: 10.1029/2018MS001583 (2019).

47. Neale, R. B. *et al.* Description of the NCAR Community Atmosphere Model (CAM 5.0). Tech. Rep. NCAR/TN-486+STR, 274 pp., National Center for Atmospheric Research (2012).

48. Samset, B. H. *et al.* Fast and slow precipitation responses to individual climate forcers: A PDRMIP multimodel study. *Geophysical Research Letters* **43**, 2782–2791, 10.1002/2016GL068064 (2016).

49. Myhre, G. *et al.* Scientific data from precipitation driver response model intercomparison project. *Scientific Data* **9**, 123, doi: 10.1038/s41597–022–01194–9 (2022).

50. Soden, B. J. *et al.* Quantifying climate feedbacks using radiative kernels. *Journal of Climate* **21**, 3504–3520, doi: 10.1175/2007JCLI2110.1 (2008).

51. Zelinka, M. D., Klein, S. A. & Hartmann, D. L. Computing and partitioning cloud feedbacks using cloud property histograms. Part I: Cloud radiative kernels. *Journal of Climate* **25**, 3715–3735, doi: 10.1175/JCLI–D–11–00248.1 (2012).

52. Ramaswamy, V. *et al.* *Radiative Forcing of Climate Change, Chapter 6 of the IPCC Third Assessment Report Climate Change 2001: The Scientific Basis.* (United States, 2001).

Figure 1 **Total climate response to methane perturbations.** Global annual mean (a) near-surface air temperature and (b) precipitation response for 2xCH_4 (first set of points), 5xCH_4 (second set of points) and 10xCH_4 (third set of points) from coupled simulations (which include the IRF, adjustments and feedbacks). Responses are decomposed into CH_{4LW+SW} (black), CH_{4LW} (red) and CH_{4SW} (blue). Also included are the least-squares regression lines (dashed). Solid circles represent a significant response at the 90% confidence level, based on a standard t-test. The thin black vertical line shows the present-day CH_4 perturbation of 1.1 ppm. Also shown is the estimated (from the regressions) present-day CH_4 climate response for (c) near-surface air temperature, (d) precipitation, and (e) apparent hydrological sensitivity. The first bar in each like-colored set of three bars represents the contribution from CH_{4LW+SW}; the second bar represents CH_{4LW}; and the third bar represents CH_{4SW} (i.e., except for (e), the CH_{4LW+SW} bar is equal to the sum of the CH_{4LW} and CH_{4SW} bar). Error bars in (c, d, e) show the 1-standard deviation uncertainty estimate of the regression slope, which is estimated from the 3 like-colored data points (CAM6 methane simulations) in (a, b). Units in (a, c) are K; units in (b) are mm day^{-1}; units in (d) are %; and units in (e) are % K^{-1}.

Figure 2 **Top-of-the-atmosphere radiative flux components and rapid adjustment decomposition for 10xCH_4.** Global annual mean top-of-the-atmosphere (TOA) (a) effective radiative forcing (ERF; black), instantaneous radiative forcing (IRF; green) and rapid adjustment (ADJ; blue) and (b) surface temperature (purple), tropospheric temperature (cyan), stratospheric temperature (yellow), water vapor (red), surface albedo (orange), cloud (pink) and total (blue) rapid adjustment for 10xCH_4. The first bar in each like-colored set of three bars represents the contribution from 10xCH_{4LW+SW}; the second bar represents 10xCH_{4LW}; and the third bar represents 10xCH_{4SW}. Responses not significant, based on a standard t-test at the 90% confidence level, have unfilled bars. Units are W m^{-2}.

Figure 3 **Global annual mean vertical profiles of fast responses for 10xCH_4.** Atmospheric (a) shortwave heating rate (QRS; [K day^{-1}]), (b) temperature (T; [K]), (c) relative humidity (RH; [%]) and (d) cloud fraction (CLOUD; [%]) for 10xCH_4. Panels include the contribution from 10xCH_{4LW+SW} (solid black); 10xCH_{4LW} (dotted); and 10xCH_{4SW} (dashed). Solid dots represent a significant response at the 90% confidence level, based on a standard t-test. Also included in (a) is the instantaneous shortwave heating rate profile (10x$CH_{4SW\text{-}IRF}$; gray).

Figure 4 **Global annual mean vertical profiles of instantaneous heating rate for 10xCH_{4SW}.** Instantaneous atmospheric (a) clear-sky shortwave heating rate (QRS IRF_{cs}; gray) and the corresponding clear-sky shortwave heating rate without water vapor shortwave absorption (QRS IRF_{cs} noH2Ov; purple) in the same three near-infrared bands (1.6-1.9, 2.15-2.5 and 3.1-3.85 μm) that methane absorbs in. Instantaneous atmospheric (b) all-sky (i.e., with clouds) shortwave heating rate (QRS IRF; as in Fig. 3a; gray) and the corresponding shortwave heating rate without water vapor shortwave absorption (QRS IRF noH2Ov; purple) in the same three near-infrared bands that methane absorbs in. Also included in (a) is the climatological specific humidity (SH; red) and in (b) the climatological cloud fraction (CLOUD; cyan). QRS IRF, QRS IRF$_{cs}$, CLOUD and SH units are K day^{-1}, K day^{-1}, % and g kg^{-1}, respectively.

Figure 5 **Top-of-the-atmosphere radiative flux decomposition for the total response, rapid adjustment and feedback for 10xCH_{4SW}.** Global annual mean top-of-the-atmosphere (TOA) surface temperature (purple), tropospheric temperature (cyan), stratospheric temperature (yellow), water vapor (red), surface albedo (orange), cloud (pink) and total (blue) radiative flux decomposition for 10xCH_{4SW}. The first bar in each like-colored set of three bars represents the total response (from the coupled ocean simulations); the second bar represents the rapid adjustment (i.e., fast response); and the third bar represents the surface-temperature induced feedback (i.e., slow response). Responses not significant, based on a standard t-test at the 90% confidence level, have unfilled bars. Units are W m^{-2}.

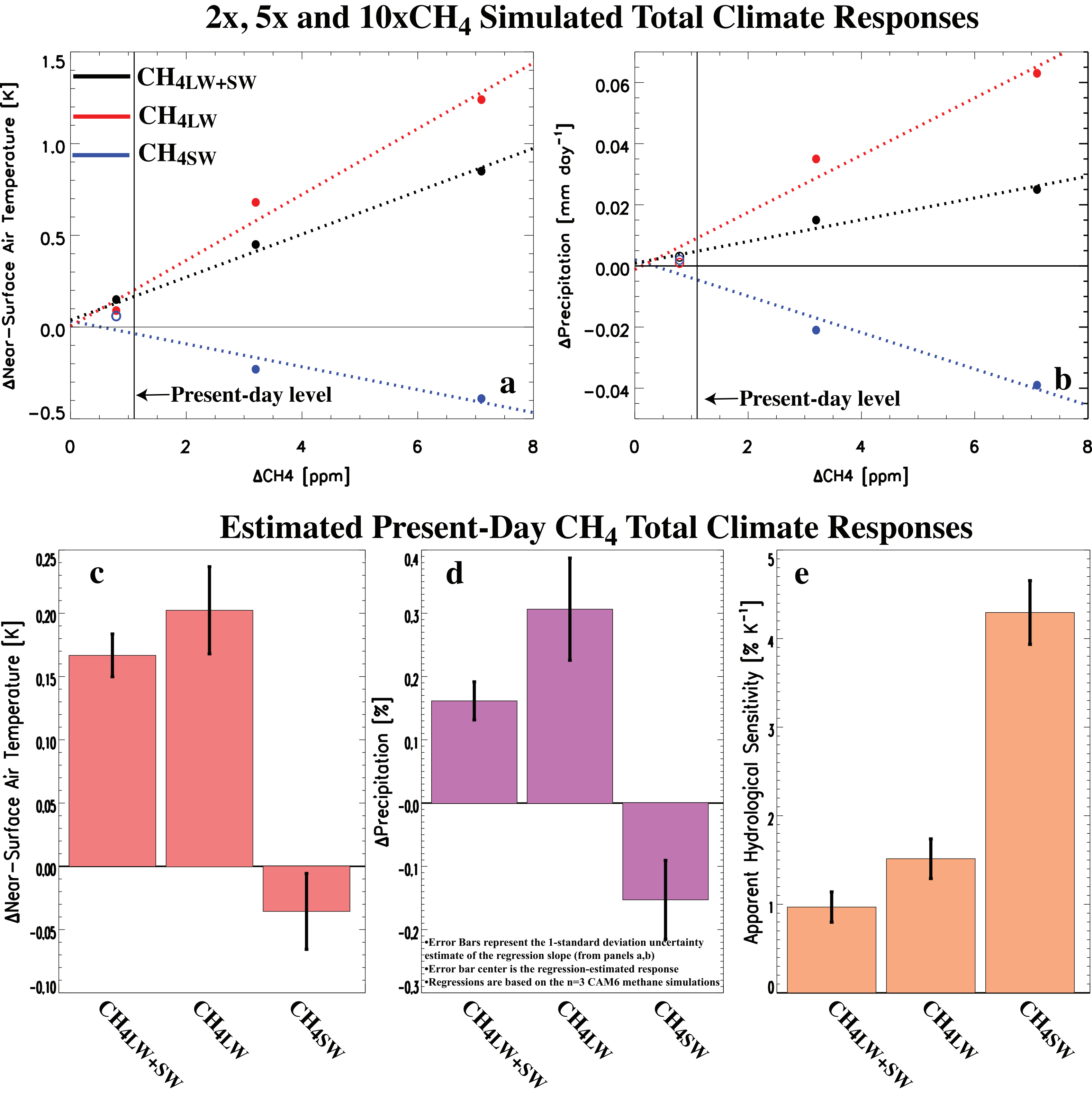

2x, 5x and 10xCH4 Simulated Total Climate Responses
CH4LW+SW
CH4LW
CH4SW
ΔNear−Surface Air Temperature [K]
Present-day level
a
ΔCH4 [ppm]
ΔPrecipitation [mm day−1]
Present-day level
b
ΔCH4 [ppm]
Estimated Present-Day CH4 Total Climate Responses
c
ΔNear−Surface Air Temperature [K]
CH4LW+SW
CH4LW
CH4SW
d
ΔPrecipitation [%]
•Error Bars represent the 1-standard deviation uncertainty estimate of the regression slope (from panels a,b)
•Error bar center is the regression-estimated response
•Regressions are based on the n=3 CAM6 methane simulations
e
Apparent Hydrological Sensitivity [% K−1]

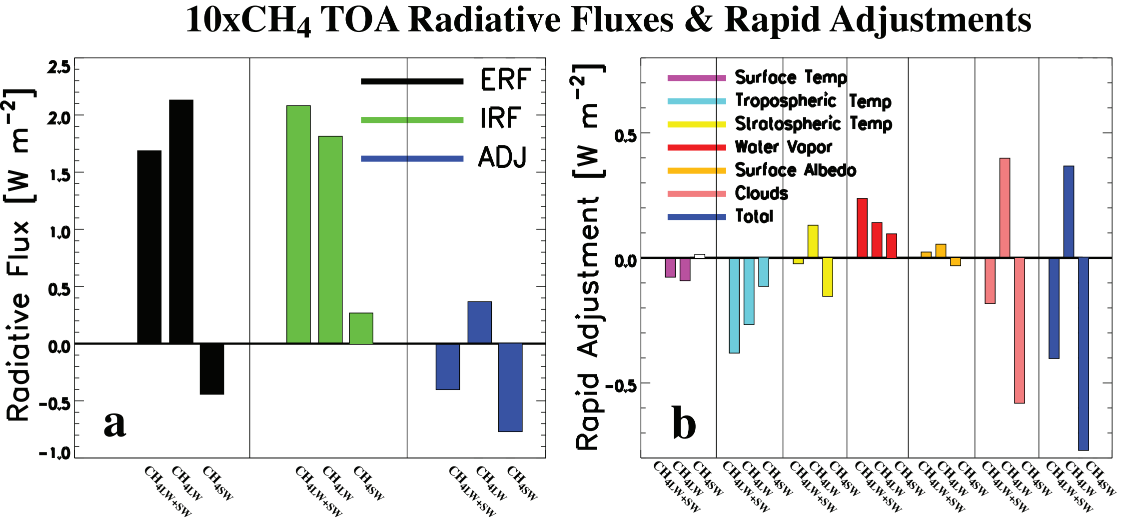

10xCH4 TOA Radiative Fluxes & Rapid Adjustments
Radiative Flux [W m−2]
2.5
2.0
1.5
1.0
0.5
0.0
-0.5
-1.0
ERF
IRF
ADJ
a
CH4LW+SW
CH4LW
CH4SW
Rapid Adjustment [W m−2]
0.5
0.0
-0.5
Surface Temp
Tropospheric Temp
Stratospheric Temp
Water Vapor
Surface Albedo
Clouds
Total
b

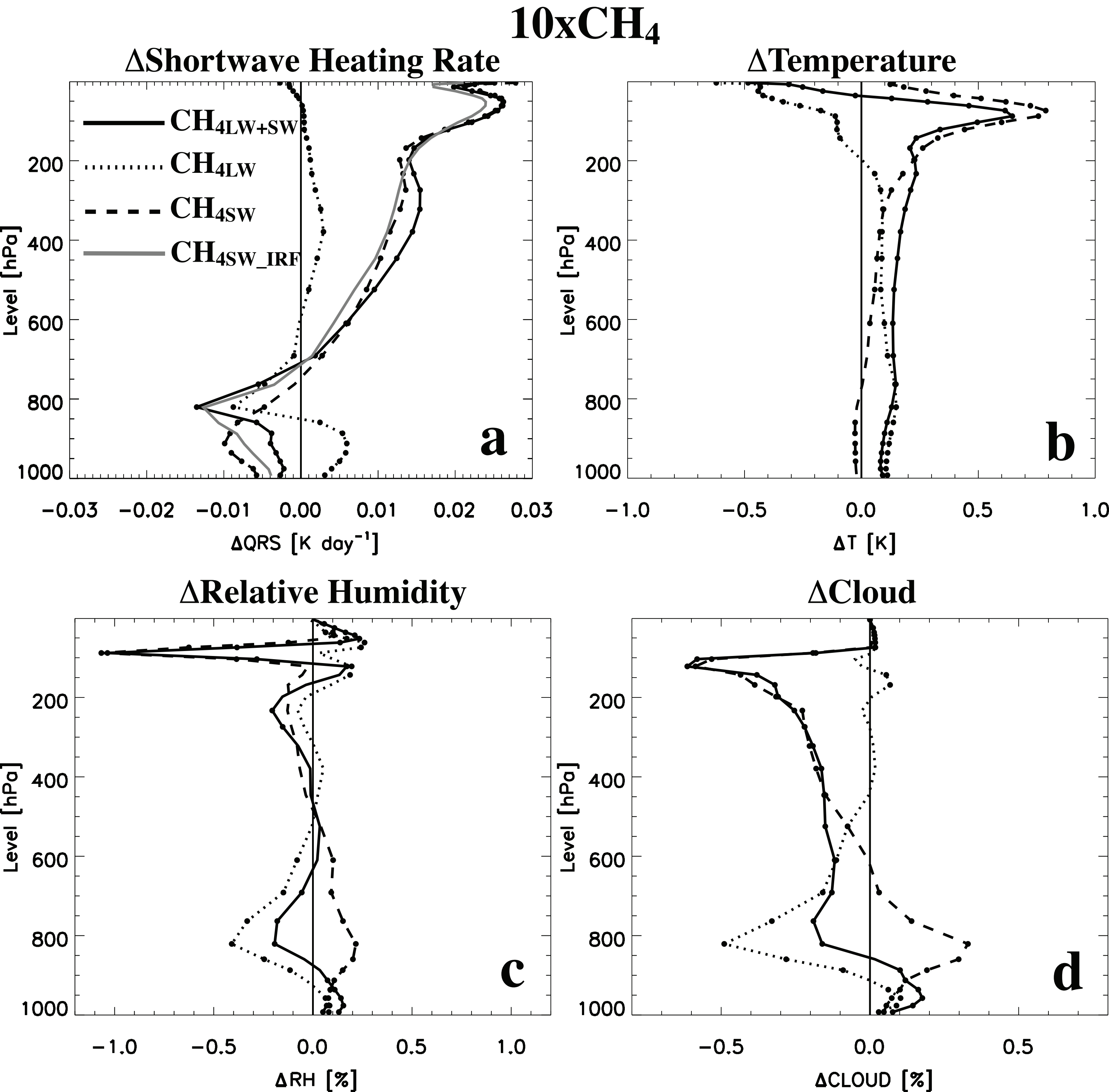

10xCH4
ΔShortwave Heating Rate
ΔTemperature
ΔRelative Humidity
ΔCloud
CH4LW+SW
CH4LW
CH4SW
CH4SW_IRF
Level [hPa]
200
400
600
800
1000
a
b
c
d
ΔQRS [K day-1]
-0.03 -0.02 -0.01 0.00 0.01 0.02 0.03
ΔT [K]
-1.0 -0.5 0.0 0.5 1.0
ΔRH [%]
-1.0 -0.5 0.0 0.5 1.0
ΔCLOUD [%]
-0.5 0.0 0.5

$10xCH_{4SW}$

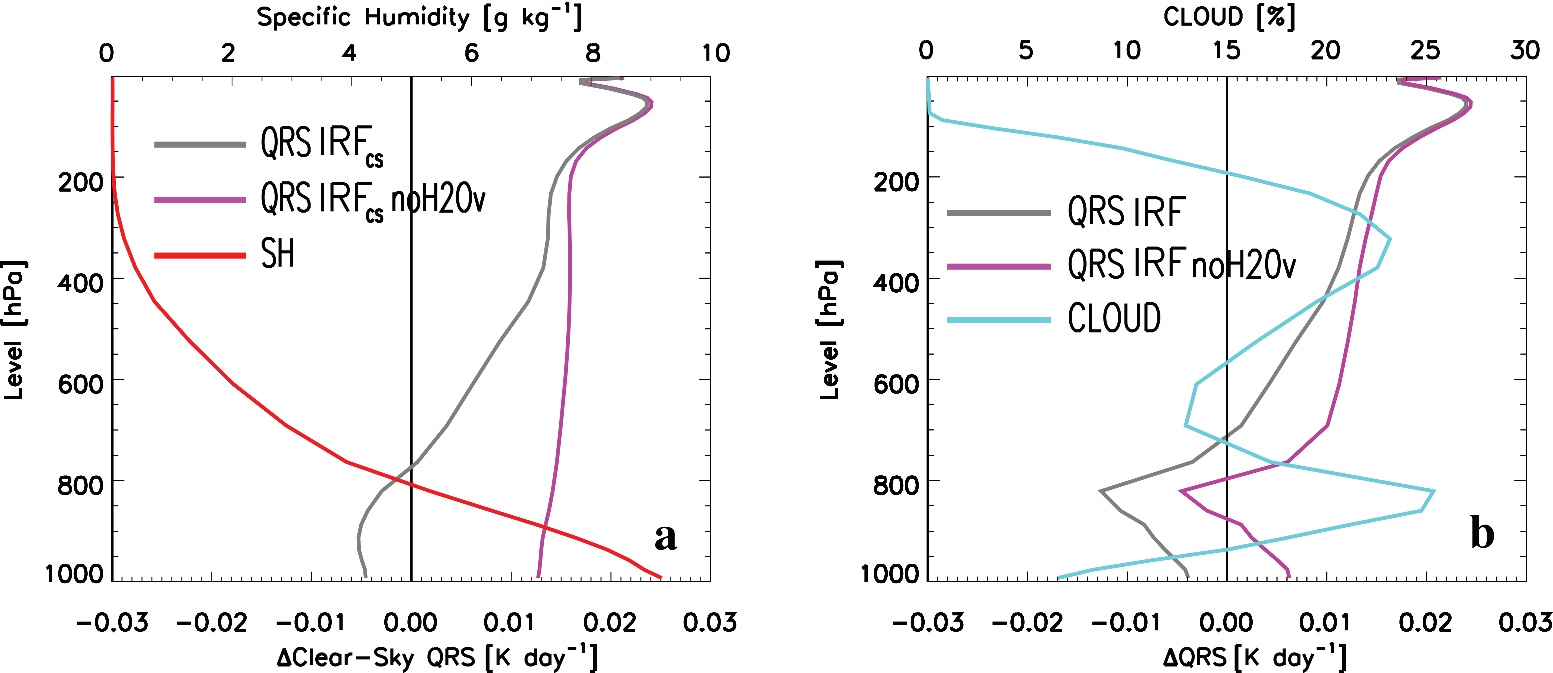

Specific Humidity [g kg^{-1}]
QRS IRF$_{cs}$
QRS IRF$_{cs}$ noH20v
SH
Level [hPa]
ΔClear−Sky QRS [K day^{-1}]
a
CLOUD [%]
QRS IRF
QRS IRF noH20v
CLOUD
Level [hPa]
ΔQRS [K day^{-1}]
b

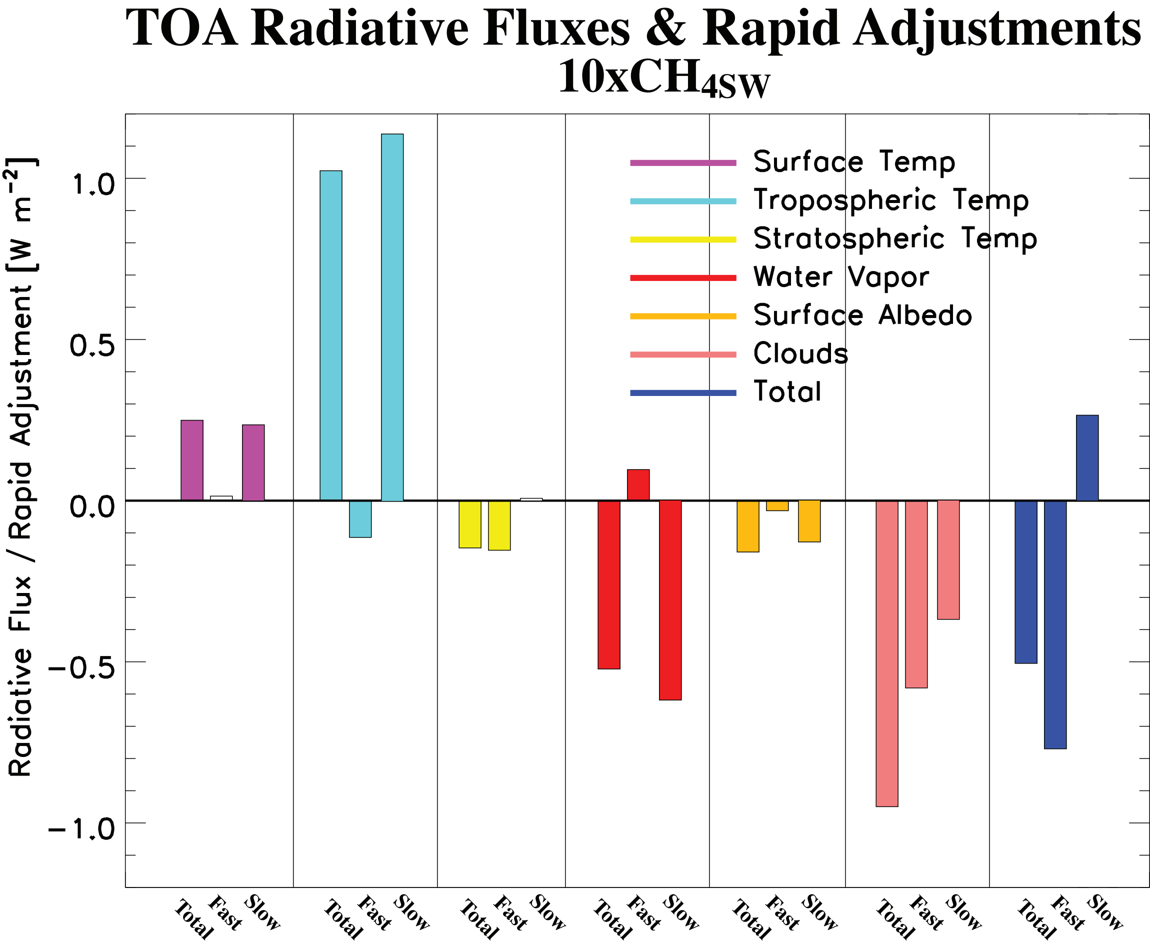

TOA Radiative Fluxes & Rapid Adjustments
10xCH4SW
Radiative Flux / Rapid Adjustment [W m−2]
1.0
0.5
0.0
−0.5
−1.0
Surface Temp
Tropospheric Temp
Stratospheric Temp
Water Vapor
Surface Albedo
Clouds
Total
Total Fast Slow
Total Fast Slow
Total Fast Slow
Total Fast Slow
Total Fast Slow
Total Fast Slow
Total Fast Slow